Journal of Engineering Mathematics **42:** 65–90, 2002.

Acoustically generated unsteady vorticity field in a long narrow cylinder with sidewall injection

KADIR KIRKKOPRU[1], DAVID R. KASSOY[2], QING ZHAO[3] and PETER L. STAAB[4]
[1]*Department of Mechanical Engineering, Istanbul Technical University,Gumussuyu, Istanbul, Turkey*
[2]*Department of Mechanical Engineering, University of Colorado, Boulder, CO 80309, U.S.A.*
[3]*AVAYA Communications, Westminster, CO 80234, U.S.A.*
[4]*Department of Mathematics, Colorado College, Colorado Springs, CO 80903, U.S.A.*

Received 3 May 2000; accepted in revised form 10 September 2001

Abstract. Asymptotic and computational analyses of a well-posed initial-boundary-value problem are used to describe the time history of co-existing acoustic and rotational velocity disturbances in a long, narrow cylinder with uniform steady sidewall mass injection. Transient planar pressure disturbances prescribed on the open exit plane of the cylinder are the source of acoustic disturbances in the axisymmetric flow. Both the asymptotic and numerical solutions describe the nonlinear aspects of the flow interactions. The full computational results are compared favorably with those of the asymptotic study to show that; (1) transient vorticity is generated near the injection surface and is transported into the cylinder by the radial velocity component of the flow field, (2) at any sufficiently small value of time, a well defined front separates the fluid containing transient vorticity from a flow field in the interior of the cylinder containing a much smaller amplitude vorticity and, (3) at sufficiently large values of time, vorticity is present throughout the cylinder. In addition, the analytically derived acoustic solution obtained from the asymptotic analysis is used to show that the present numerical solution and all earlier studies of similar problems are missing travelling waves (eigenfunctions) which should be present in a complete mathematical solution of the defined initial-boundary-value problem.

Key words: asymptotics, computational, cylinder, low-Mach-number flow, sidewall mass addition.

1. Introduction

This modeling study elucidates some of the fundamental properties of co-existing, interacting acoustic and vorticity disturbances in a high-Reynolds-number, low-Mach-number flow. The geometrical context is a long, relatively narrow cylinder with one open end and uniform, steady mass injection from the porous sidewall. An acoustic field, induced by an imposed pressure transient on the exit plane, interacts with the injected fluid to create intense, transient vorticity on the porous surface. Subsequently, radial and axial convection combine with radial diffusion to distribute the vorticity throughout the cylinder.

The flow configuration chosen is an idealization of that found in a solid rocket motor. Sidewall mass injection is used to model the normal velocity of gaseous products generated by combustion of gasified propellant in an extremely thin reaction zone adjacent to the degrading solid material. The exit-plane pressure transient is used to disturb the flow system in a deterministic way. This application provides a useful testbed for studying the time-dependent dynamics of mixed irrotational and rotational flow fields. The modeling approach and the results may be useful in other applications where acoustic disturbances are present in transient shear flows and, particularly, in turbulent flows.

Mathematical modeling of the flow system is developed in terms of an initial-boundary value problem (IBVP), derived from the nondimensionalized Navier–Stokes equations with relevant boundary and initial conditions. Asymptotic and computational methods are used to derive general transient solutions that describe the evolution of the flow field. Comparisons of the analytical and numerical solutions are used to identify limitations in past and present computational predictions of the flow-field pressure transients.

A variety of related computational, quasi-analytical and experimental studies have been carried out in the past to describe these phenomena. Vuillot and Avalon [1] provide a numerical solution to the compressible Navier–Stokes equations in a two-dimensional, long, narrow channel (the ratio of length to half height $\delta = 10$) with uniform sidewall mass injection. A harmonic pressure transient, 5% of the mean pressure, is imposed at the exit plane to create an acoustic field in the cylinder. The flow Reynolds number based on the characteristic axial velocity and the channel length is $\mathrm{Re} \approx 3 \times 10^3$ and the characteristic axial Mach number is $M \approx 0{\cdot}1$. Solutions for time scales measured by the axial acoustic time, t'_a (the ratio of the length to the characteristic acoustic speed), predict that unsteady vorticity is confined to a region between the sidewall and half the cylinder radius. The computational acoustic pressure field is harmonic at the forced frequency. Vuillot [23] re-emphasizes the importance of vorticity in these unsteady injected internal flows.

Later, Smith *et al.* [2] do a numerical simulation of Brown *et al.*'s [3, 4] cold flow experiments in a long cylinder ($\delta = 38{\cdot}4$) with an attached short nozzle, based on the compressible Navier-Stokes equations. The steady flow due to uniform sidewall injection (characteristic axial Mach number $M \approx 0{\cdot}1$ and corresponding Reynolds number based on the cylinder length $\mathrm{Re} \approx 3 \times 10^6$) is disturbed by imposed harmonic mass injection from the wall at a single location just before the nozzle. The predicted transient acoustic pressure amplitude is 0·5% of the mean pressure and composed only of the forced mode. The essential features of the rotational unsteady flow, observed by Brown *et al.* [3, 4], are predicted.

Tseng *et al.* [5] use the Navier-Stokes equations to develop a computational solution for uniform injected flow in a channel, which includes the effect of a thin classical flame located adjacent to the sidewall. A 2% harmonic pressure disturbance is applied on either an exit plane or endwall boundary to generate the acoustic field. In order to resolve the flame, nonuniform gridding is clustered near the injecting wall of a large aspect ratio ($\delta = 20$) planar chamber without a nozzle. Time-averaged results are used to show that vorticity is present only very close to the wall where the flame is located.

Roh and Yang [6] do similar computations for a system with double-base solid-propellant combustion. Longer run times, but still on the t'_a scale, and improved radial spatial resolution lead to the appearance of vorticity through 75% of the half height of the rectangular chamber.

Unlike the previously described studies based on a uniform distribution of injected fluid from the sidewall, Kirkkopru *et al.* [7] develop an initial-value numerical solution for the flow in a cylinder with transient, spatially distributed mass injection. In this case, the unsteady injection is the direct source of an acoustic disturbance field in the cylinder. Transient solutions are employed to show how unsteady vorticity generated along the sidewall convects away from the wall, eventually filling the entire cylinder. Here again, the acoustic pressure field contains only the forcing frequency of the imposed spatially varying harmonic sidewall fluid injection. In contrast, the analogous, formal acoustic solution in the IBVP given by Staab *et al.* [8], indicates that non-dissipating eigenfunctions should be present on the time scales of interest.

Flandro [9] formulates an innovative linear analytical theory based on an inviscid equation, to describe the spatial distribution of unsteady vorticity arising in an acoustic boundary layer.

The assumed acoustic pressure field is quasi-steady and infinitesimally small in the linear stability formulation employed. A systematic evaluation of the asymptotic method used to construct the model shows that the amplitude of the pressure disturbance is limited to less than 0·1% of the base value, for the parameters chosen.

Flandro and Roach [10] develop an analytical model to describe the experiments of Brown *et al.* [3, 4], which can be compared with the computational study by Smith *et al.* [2]. The model has the inherent limitations of the earlier work by Flandro [9]. Widespread small-amplitude unsteady vorticity is predicted. Flandro [11] uses a related formulation to develop a theory where co-existing vorticity and acoustics are present throughout the flow field. The steady, inviscid rotational Culick [12] solution, associated with a uniform injection Mach number, $M_b \ll 1$, is disturbed by a smaller $O(\epsilon)$ assumed harmonic acoustic velocity (and pressure). A linear stability approach is used to derive an inviscid, linear small-disturbance equation that describes the rotational flow field with an assumed quasi-steady time variation. This model retains viscosity, which has a minor effect on the vorticity distribution, given the cited parameter values.

Majdalani and Van Moorhem [13] use the basic small-disturbance, linear stability theory of Flandro [11] to describe stronger effects of viscosity on the unsteady vorticity. The infinitesimally small-pressure disturbance is assumed to be quasi-steady along with all of the other dependent-variable responses. Related modeling is given by Majdalani *et al.* [14] and Majdalani [15] who have compared their results with those of Flandro [11], and Majdalani and Van Moorhem [13].

Casalis *et al.* [24] and Avalon *et al.* [25] have included rotational disturbances in a purely hydrodynamic stability study of planar flow in a channel with steady sidewall injection. Non-parallel stability theory is used to do a linear analysis of the steady solution. Results are sensitive to the transverse velocity component of the steady flow and demonstrate the importance of non-parallel effects.

It should be stressed that all of the previously cited analytical studies employ some form of linear stability analysis for infinitesimal disturbances in which the quasi-steady acoustic field is assumed, rather than being calculated from some prescribed boundary disturbances. The problem formulation of Kassoy and co-workers [7, 8, 16, 17] is more closely related to the IBVP approach used in the computational work mentioned earlier. They formulate an initial-boundary-value theory for a weakly nonlinear and viscous flow process where relatively larger transients are introduced by imposing significant disturbances on a boundary. The acoustic field is calculated, rather than assumed. Transient variations in axial velocity are as large in amplitude as the steady Culick [12] value, which exists when the transient boundary disturbances are absent and only a uniform steady injection from the sidewall is present. Typical pressure transients in the asymptotic analyses are up to about 10% of the base value, nearly a hundred times larger than that in the stability-based theories.

Staab *et al.* [8] use a formal multiple-scale asymptotic method to study an internal axisymmetric unsteady flow driven by a time-dependent injection distribution along the sidewall of the cylinder. A balance of nonlinear convection and viscous diffusion controls the evolution of the unsteady vorticity distribution in the cylinder. A comparison of asymptotic results for this transient sidewall injection initial-boundary-value problem with those from Kirkkopru *et al.*'s [7] numerics given in Figure 8 in [8] shows quite good quantitative agreement for the instantaneous radial variation of the rotational axial velocity component. However, notable differences near the sidewall are attributed to the missing eigenfunction pressure response in the full numerical computations.

The present work employs computational and asymptotic analyses to develop transient solutions for flow in a cylinder with uniform wall injection and a prescribed small, but finite, pressure disturbance on the exit plane, similar to that used by Vuillot and Avalon [1]. The disturbance amplitude is compatible with a nonlinear treatment of the flow process. Results are obtained for axial Reynolds numbers in the range $3 \times 10^4 - 3 \times 10^5$ and for axial Mach numbers in the range $2 \times 10^{-2} - 10^{-1}$. Unlike earlier computational studies [1, 2, 5, 6] of this type of problem, radial grid distributions are based on the scaling results from asymptotic studies [8, 16, 17]. As a result, small wave-length phenomena in the numerical solutions are more accurately resolved in the core of the cylinder than was possible in the past. The MacCormack explicit predictor-corrector method [18] is used to obtain solutions to the compressible Navier–Stokes equations in which demonstrably small axial viscous stresses and conduction terms are neglected. Concepts derived from asymptotic studies [8, 16, 17] are used to split the numerical axial velocity into separate steady, acoustic and transient rotational components. Spatially resolved, time-dependent results are used to describe the transient vorticity distribution in the entire cylinder.

The asymptotic method of Zhao *et al.* [17] and Staab *et al.* [8] features the use of limit process expansions and multiple-scale methods based on a single limit, $M \to 0$ where Re and δ are defined as specific functions of M, so that the order of each term in the Navier–Stokes equations is clearly defined. The reduced equations are independent of small parameters. A formal, standard multiple-scale approach is used because physical processes occur simultaneously on two different radial leghth scales, namely the radius of the cylinder and an $O(M)$ smaller length. First, a linear acoustic solution, driven by the imposed, finite, exit-plane harmonic pressure disturbance is derived. The acoustic pressure field is shown to contain an infinite number of eigenfunctions in addition to the forced mode, for the acoustic time scales considered in the study. Secondly, a weakly nonlinear convection-diffusion equation is solved to obtain the rotational component of the axial velocity. Unlike the linear stability theories [9–11, 13–15], the amplitude of the transient axial velocity (acoustic + rotational components) is the same order of magnitude as the steady Culick [12] profile resulting from uniform injection from the sidewall.

A comparison of the fully computational solutions with those found from the multiple-scale, asymptotic study confirms many of the characteristic features of the flow field discussed here and in the References 8, 16 and 17. However, the comparison also illuminates a basic deficiency in previous computational solutions cited above, as well as that given here. Each predicts only the forced harmonic component of the acoustic pressure field, regardless of the source of forcing. In contrast, all of the asymptotic analyses demonstrate that nondissipating eigenfrequency modes are present in the acoustic field, in addition to the forced mode. The sources and consequences of this difference, not previously noted in the literature, are considered in Sections 3–5.

The work presented here provides a systematic, nonlinear mathematical analysis of relatively large, co-existing acoustic and rotational flow-field disturbances. Asymptotic and computational methods have been employed to develop transient solutions to a well-posed IBVP. Analytical insights have been used to facilitate the computational study and understand its limitations. The results enable one to understand the source and evolution of vorticity in the system, its ultimate distribution and the length scales on which it is important. These insights represent the fundamental contribution of the present work.

2. Mathematical model

An initial-boundary-value problem (IBVP) is defined in terms of the cylindrical, axisymmetric, laminar, compressible Navier–Stokes equations, written in nondimensional conservative form as;

$$\frac{\partial q}{\partial t} + \frac{\partial e}{\partial x} + \frac{\partial f}{\partial r} + \frac{h}{r} = 0 \tag{1}$$

where

$$q = \begin{pmatrix} \rho \\ E_T \\ \rho u \\ \rho v \end{pmatrix}, \qquad e = \begin{pmatrix} M\rho u \\ M[E_T + (\gamma - 1)p]u \\ M\rho u^2 + \frac{1}{\gamma M} p \\ M\rho uv \end{pmatrix},$$

$$f = \begin{pmatrix} M\rho v \\ M[E_T + (\gamma - 1)p]v - \frac{\gamma M \delta^2}{\mathrm{RePr}} T_{,r} \\ M\rho uv - \frac{M\delta^2}{\mathrm{Re}} u_{,r} \\ M\rho v^2 + \frac{\delta^2}{\gamma M} p \end{pmatrix}, \quad h = \begin{pmatrix} M\rho v \\ M[E_T + (\gamma - 1)p]v - \frac{\gamma M \delta^2}{\mathrm{RePr}} T_{,r} \\ M\rho uv - \frac{M\delta^2}{\mathrm{Re}} u_{,r} \\ M\rho v^2 \end{pmatrix}. \tag{2}$$

The equation of state for a perfect gas is

$$p = \rho T. \tag{3}$$

The nondimensional initial conditions are given by the steady-state values for u, v, p, ρ and T to be calculated subject to a specified injection velocity ($v = -1$), temperature ($T = 1$) and no-slip condition for the axial flow velocity ($u = 0$) on the injecting side wall at ($r = 1$), symmetry conditions at ($r = 0$), an impermeable wall ($u = 0$) at $x = 0$ and a steady static pressure condition ($p = 1$) at the open end $x = 1$. The boundary conditions for the IVBP are the same as those for initial conditions, except the unsteady static pressure condition at the exit plane ($x = 1$), $p = 1 + A \sin \omega t$, where ω is the dimensionless angular frequency and A is the amplitude of the pressure oscillation.

Nondimensional variables, defined in terms of primed dimensional quantities, are given by

$$\begin{aligned} x &= x'/L', \quad r = r'/R', \quad u = u'/U'_R, \quad v = v'/V'_R, \quad p = p'/p'_0, \\ \rho &= \rho'/\rho'_0, \quad T = T'/T'_0, \quad t = t'/t'_a, \quad C_v = C'_v/C'_{v0}. \end{aligned} \tag{4}$$

Characteristic length scales for the axial and radial directions are chosen to be the length of the tube L' and the radius of the tube R', respectively. The characteristic sidewall injection speed of the fluid V'_R is related to the characteristic mean axial speed U'_R through the global mass conservation relationship $U'_R = \delta V'_R$, where $\delta = L'/R'$ is the aspect ratio of the tube. The reference value p'_0 is the initial static pressure in the cylinder, while the analogous density and temperature values ρ'_0 and T'_0, respectively, represent properties of the injected fluid. Time is nondimensionalized with respect to the tube axial acoustic time $t'_a = L'/a'_0$, where $a'_0 = (\gamma p'_0/\rho'_0)^{1/2}$ is the characteristic speed of sound. Here, the ratio of specific heats $\gamma = 1{\cdot}4$. The viscosity, specific heats and conductivity are treated as constants in these calculations because temperature variations are very small.

The Reynolds number, the Prandtl number and the mean axial flow Mach number, respectively, are defined by

$$\mathrm{Re} = \frac{\rho_0' U_R' L'}{\mu_0'}, \qquad \mathrm{Pr} = \frac{\mu_0' C_{po}'}{k_o'}, \qquad M = \frac{U_R'}{a_o'}. \tag{5}$$

Typical parameter values are $\mathrm{Re} = O(10^5 - 10^6)$, $\mathrm{Pr} = O(1)$, $M = O(10^{-2} - 10^{-1})$ and $\delta = O(10)$.

Finally,

$$E_T = \rho C_v T + \gamma(\gamma - 1) M^2 \rho \frac{\left[u^2 + (v/\delta)^2\right]}{2} \tag{6}$$

represents the nondimensional form of the total energy of the fluid.

The Navier–Stokes equations are simplified by ignoring the axial viscous stress and the axial conduction. The nondimensionalization defined in (4), and used by Staab *et al.* [8] and Zhao *et al.* [17], can be used to show that these small transport effects are $O(M/\mathrm{Re})$ compared to the $O(1)$ terms in (2). Given the parameter ranges specified below (5), the magnitude of M/Re can be no larger than $O(10^{-6})$. This suggests that there is little risk in simplifying the basic equation model. The computation time for the simplified equations is reduced drastically without sacrificing the flow physics. Furthermore, the dissipative effects of the remaining transport terms are sufficient to avoid the need for artificial damping terms. This approximation has been used succesfully in earlier related work [7].

The IBVP defined in (1)–(3) will be solved using asymptotic methods based on the limit $M \to 0$ with $\mathrm{Re} \to \infty$ and then with a computational approach based on the MacCormack explicit predictor-corrector scheme [18]. Scaling and other insights about the physical characteristics of the flow obtained from the analysis are used to improve the resolution of the latter and to interpret the numerical results.

The solution strategies for both the analysis and the compuation are quite similar. First, a steady-state solution for velocity and pressure is obtained in the absence of a time-dependent pressure oscillation on the exit plane. Then, the steady flow is disturbed by the exit-plane disturbance given below (3) and a complete initial-value problem is solved. The transient velocity response is split into irrotational and rotational fields in order to distinguish acoustic transients and those associated with vorticity. The time history of the spatial distributions of the acoustic velocity and pressure, as well as the rotational velocity and the related vorticity, are obtained from each solution method, interpreted and compared.

3. Asymptotic formulation

Asymptotic analysis of the IBVP defined by (1)–(3) and associated initial and boundary conditions is based on the methods described in detail by Zhao *et al.* [17]. The summary provided below will enable the reader to understand the formulation of the acoustic problem and the subsequent development of the submodel describing the origin, transport and evolution of vorticity.

Asymptotic expansions for the dependent variables, valid in the limit $M \to 0$, are written as

$$u(x, r, t) \sim u_S(x, r) + \sum_{n=0} M^n u_n(x, r, t), \tag{7}$$

$$v(x, r, t) \sim v_S(x, r) + \sum_{n=0} M^n v_n(x, r, t), \tag{8}$$

$$(p, \rho, T) \sim 1 + M \sum_{n=0} M^n (P_n, R_n, \theta_n), \tag{9}$$

where, $u_S = \pi x \cos\left[(\pi/2)\, r^2\right]$ and $v_S = -(1/r) \sin\left[(\pi/2)\, r^2\right]$ represent steady rotational solutions to the Euler equations [12, 26]. The subscript n labels time-dependent terms in the expansions. It should be noted that the largest time-dependent velocity term u_0, a result of the $O(M)$ pressure disturbance on the exit plane, is of the same order of magnitude as the steady contribution u_S. It is implicit in the asymptotic analysis that the large aspect ratio is defined by $M\delta = O(1)$.

The early asymptotic study by Zhao and Kassoy [16], later improvements by Zhao *et al.* [17] and the computational study by Kirkkopru *et al.* [7] demonstrate that two distinct radial length scales are needed to fully resolve the flow dynamics. Important radial gradients of the axial velocity occur simultaneously on both the scale of the cylinder radius and a much shorter scale associated with the radial distance traveled by an injected fluid particle on the acoustic time scale. In mathematical terms, a multiple-scale analysis is carried out in the variables r_1 and r_2 defined by

$$r_1 = 1 - r, \qquad r_2 = \int_0^{r_1} \frac{1}{-M v_S(\sigma)} \mathrm{d}\sigma, \tag{10}$$

where the latter of (10) is an integral representation of the shorter length scale. The mathematical consequence is that several partial differential equations are simplified by the removal of the variable coefficient $v_S(r_1)$. In addition, the integral has a physical interpretation because it also defines the nondimensional time required by an injected fluid particle to move from the wall at $r_1 = 0$ to any specified radial location $r_1 > 0$. It should be noted that r_2 is unbounded in the limit $r_1 \to 1$ because of the asymptotic behavior of v_S near the centerline ($r_1 = 1$) of the cylinder.

Variable splitting of Lagerstrom [20, pp. 90–92] is used in (7)–(9) to separate irrotational and rotational components of the velocity fields. Velocities and the pressure approximations relevant to the present work can be written as

$$\begin{aligned} u_0(x, r, t) &= u_{0P}(x, t) + u_{0V}(x, t, r_1, r_2), \\ u_1(x, r, t) &= u_{1P}(x, t) + u_{1V}(x, t, r_1, r_2), \\ v_0 = 0, &\qquad P_0 = P_0(x, t), \end{aligned} \tag{11}$$

where the dependence of rotational velocity components on the multiple length scales r_1 and r_2 are shown. The pressure field is independent of the radial variable, which is a consequence of the large aspect ratio condition specified previously.

The acoustic variables u_{0P} and P_0 are described by

$$\frac{\partial^2 P_0}{\partial t^2} = \frac{\partial^2 P_0}{\partial x^2}, \quad \frac{\partial u_{0P}}{\partial t} = -\frac{1}{\gamma} \frac{\partial P_0}{\partial x}, \tag{12, 13}$$

which must satisfy the boundary and initial conditions

$$P_{0,x}(x = 0, t) = 0, \qquad P_0(x = 1, t) = A/M \sin \omega t \quad \text{for } t > 0$$

$$P_0(x,0) = P_{0,t}(x,0) = u_{0P}(x,0) = 0 \quad \text{for } t = 0, \tag{14}$$

where $A = MA^*$.

Nonresonant solutions to the acoustic equations

$$P_0(x,t) = A^* \sin \omega t + A^* \sum_{n=0}^{\infty} (-1)^n \frac{2\omega}{\lambda_n^2 - \omega^2} \left(-\sin \lambda_n t + \frac{\omega}{\lambda_n} \sin \omega t \right) \cos \lambda_n x,$$

$$u_{0P}(x,t) = \frac{A^*}{\gamma} \sum_{n=0}^{\infty} (-1)^n \frac{2\omega}{\lambda_n^2 - \omega^2} (\cos \lambda_n t - \cos \omega t) \sin \lambda_n x, \tag{15}$$

are composites of standing waves responding at the forcing frequency ω and traveling waves denoted by eigenvalues, $\lambda_n = (n + 1/2)\,\pi \neq \omega$. The eigenfunctions in (15) are a characteristic feature of solutions obtained from an asymptotic formulation of the internal flow problem with sidewall mass addition [8, 17]. Analogous computational solutions, carried out on the same time scale, contain only the forced modes [1, 2, 5–7]. This apparent deficiency in the numerical results is considered in a later section.

The rotational component of the axial velocity transient, u_{0V}, is described initially by a linear first-order wave equation;

$$\frac{\partial u_{0V}}{\partial t} + \frac{\partial u_{0V}}{\partial r_2} = 0 \tag{16}$$

and the no-slip boundary condition at the side wall $r_1 = r_2 = 0$:

$$u_{0V} = -u_{0P}(x,t). \tag{17}$$

Conceptually, the boundary conditions show how the acoustic disturbance is a driver for the rotational axial velocity field. Only a partial solution can be obtained because of the multiple-scale character of the analysis;

$$u_{0V}(x, t^*, r_1 = 0) = 0 \quad \text{for} \quad t^* \leq 0,$$

$$u_{0V}(x, t^*, r_1 = 0) = -u_{0P}(t^*, x) \quad \text{for} \quad t^* > 0, \tag{18}$$

where $t^* = t - r_2$ is a characteristic of the wave equation. The integral transformation in (10) can be used to show that the lines move radially at the local value of the steady radial velocity, $v_S(r_1)$ defined below (9).

Equation (18) demonstrates that the u_{0V} solution is preserved on characteristic lines $t^* =$ constant. It varies from the wall value defined in (18) ($t^* = t$) to zero at the front location $t^* = 0$. At the latter location, $r_{2F} = t$, (10) can be used to find the value of the original nondimensional radial variable;

$$r_F = \left[\frac{4}{\pi} \tan^{-1} \left(\mathrm{e}^{-\pi M t} \right) \right]^{1/2}, \tag{19}$$

where $Mt = t'/(L'/U'_R)$ represents the nondimensional time defined with respect to the characteristic axial flow time in the cylinder. For small elapsed times, $Mt \ll 1$, $r_F = 1 - Mt + \cdots$, implying that the front moves at the constant wall injection speed. When the elapsed time is

large, $Mt \gg 1$, $r_F \to 0$, showing that the front location only asymptotes to the centerline of the cylinder as the value of v_S below (9) aymptotes to zero.

Equations (13), (16), and (14) can be combined to show that on the wall, $r_1 = r_2 = 0$,

$$\frac{\partial u_{0V}}{\partial r_2} = -\frac{1}{\gamma}\frac{\partial P_0}{\partial x}, \tag{20}$$

which shows that the vorticity, represented by the radial gradient of u_{0V}, is created on the boundary by an interaction between the injected fluid and the axial pressure gradient arising from the time-dependent component of the pressure oscillation at the exit plane. From a conceptual perspective, (20) shows that any acoustic disturbance, represented by the axial pressure gradient, will be the source of vorticity. Thus, the result in (15), arising from the model exit-plane boundary condition can be replaced by any other acoustic solution relevant to a specific geometrical configuration.

The multiple-scale analysis is extended by finding the wave equation for u_{1V};

$$\frac{\partial u_{1V}}{\partial t} + \frac{\partial u_{1V}}{\partial r_2} = N_1, \tag{21}$$

where N_1 is a nonlinear function of u_{0V} and other lower-order dependent variables and explicitly contains viscous terms. The appearence of the latter at this order of the analysis requires the parameter relationship, $\delta^2/\mathrm{Re}\,M^2 = \mathrm{O}(1)$. When combined with the aforementioned large-aspect-ratio condition in $M\delta = O(1)$, it follows that $\mathrm{Re} = O(M^{-4}) \gg 1$ in the small-Mach-number limit.

The particular solution to (21), $u_{1Vp}(x, t^*, r_1, r_2)$, will contain secular terms in t^*, unless specific terms in N_1 are suppressed. It follows that a complete solution for $u_{0V}(x, t, r_1, r_2)$ is described by

$$0 = \frac{\delta^2}{\mathrm{Re}\,M^2}\frac{1}{v_S^2}\frac{\partial^2 u_{0V}}{\partial r_2^2} - \frac{\partial}{\partial x}\left[u_{0V}\left(\frac{1}{2}u_{0V} + u_S\right)\right] + v_S\frac{\partial u_{0V}}{\partial r_1}, \tag{22}$$

the initial condition in (18) and the boundary conditions

$$u_{0V}(0, r_1, r_2, t) = 0, \qquad \frac{\partial u_{0V}}{\partial r_2}(x, r_1 \to 1, r_2 \to \infty, t) = 0. \tag{23}$$

Equation (22) is a nonlinear convection-diffusion equation that defines the properties of u_{0V} at time t, in the region between the wall and the vicinity of the front $r_F = t$, $0 \le r_2 \approx t = r_F$. The solution describes how vorticity created at the wall in (20) is convected axially, and radially with respect to the r_1 variable, while being diffused with respect to the r_2 variable. The method of lines is used to obtain a solution to the IBVP defined by (22) and the associated initial and boundary conditions.

It is worthwhile to note that the axial velocity transient, $u_{0P}+u_{0V}$, arising from the imposed exit-plane $O(M)$ pressure disturbance is of the same order of magnitude as u_S in (7). In contrast, the linear stability studies in the References [9, 11, 13–15] describe axial velocity transients that are very small compared to the steady Culick [12] value.

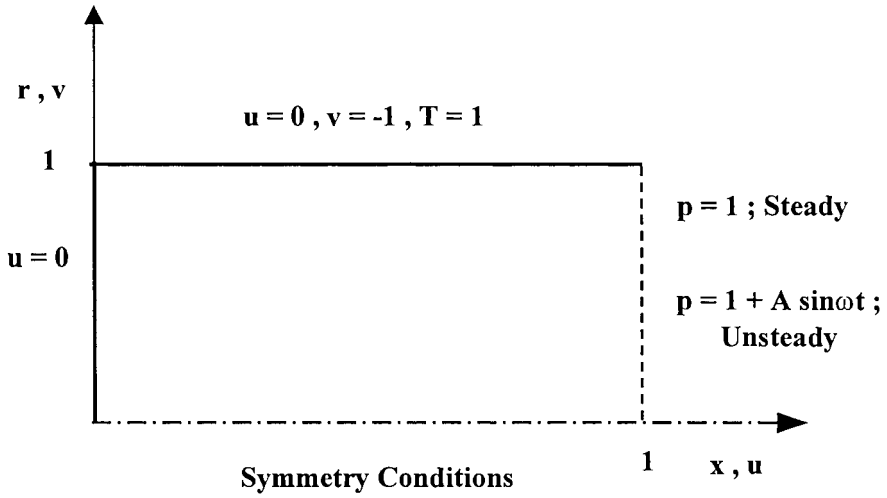

Figure 1. Computational domain and boundary conditions.

4. Computational formulation

The IBVP defined by (1–3) and associated initial and boundary conditions is solved by use of the MacCormack explicit, predictor-corrector scheme [18].

$$\overline{q}_{i,j} = q^n_{i,j} - \frac{\Delta t}{\Delta x}(e^n_{i+1,j} - e^n_{i,j}) - \frac{\Delta t}{\Delta r}(f^n_{i,j+1} - f^n_{i,j}) - \frac{\Delta t}{r}h^n_{i,j},$$
$$q^{n+1}_{i,j} = \frac{1}{2}\left[q^n_{i,j} + \overline{q}_{i,j} - \frac{\Delta t}{\Delta x}\left(\overline{e}_{i,j} - \overline{e}_{i-1,j}\right) - \frac{\Delta t}{\Delta r}\left(\overline{f}_{i,j} - \overline{f}_{i,j-1}\right) - \frac{\Delta t}{r}\overline{h}_{i,j}\right]. \qquad (24)$$

Here, the overbar denotes the predictor stage, while the superscripts n and $n+1$ represent the known and unknown time levels, respectively, separated by Δt. The subscripts i and j refer to axial and radial directions, respectively.

The computational domain shown in Figure 1 is used to represent the axisymmetric system. The injected fluid speed on the cylinder wall is constant. The left side of the cylinder is a closed rigid wall and the right side is a flow exit plane, where a specific transient pressure variation is imposed.

The aspect ratio is $\delta = 20$ for all present computations. Grid points are equally spaced in each direction and the radial grid size is dependent on the value of M.

4.1. Steady-state computations

The IBVP is first solved for the steady-state boundary conditions. Radial viscous terms are retained so that one finds the viscous analogues to the Culick solutions defined below (9). Retention of the radial derivatives also helps to accelerate the convergence to steady state by providing physically meaningful damping of numerical disturbances.

A steady-state flow solution is required as an initial condition for the transient-flow computation. Boundary conditions include an impermeable wall at $x = 0$ ($u = 0$), a static pressure condition at the open end $x = 1$ ($p = 1$), a specified injection velocity ($v = -1$), temperature ($T = 1$) and no-slip condition for the axial flow speed ($u = 0$) on the injecting upper sidewall at $r = 1$ and symmetry conditions on the lower (centerline) boundary, $r = 0$.

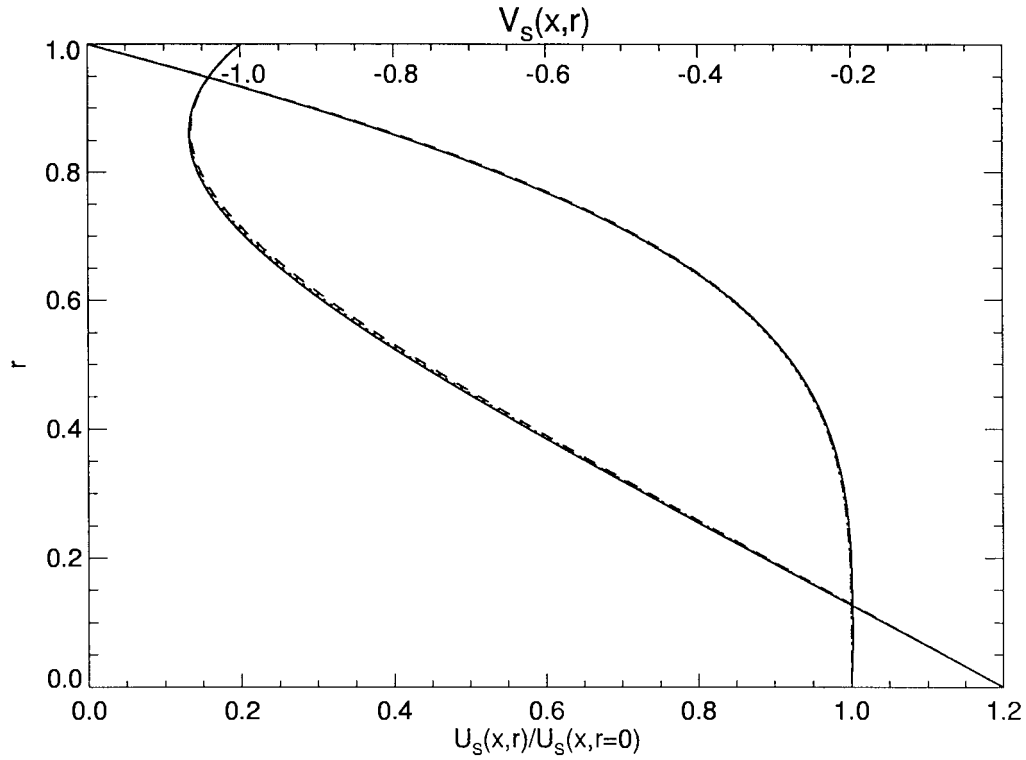

Figure 2. Normalized steady axial velocity and steady radial velocity profiles at $x = 0{\cdot}025$ (solid line), $0{\cdot}5$ (dotted line) and 1 (dashed line) for $M = 0{\cdot}05$ and $\mathrm{Re} = 3 \times 10^5$.

The analytically calculated velocity profiles for incompressible, inviscid, rotational flow in a long, narrow cylindrical tube (Culick [12]) are used as starting conditions for the steady, compressible, viscous-flow computations. This approach leads to the final converged steady-flow configuration in an efficient manner. In this calculation, the solution converges to a steady state defined by the condition that the total injected mass is equal to the total exiting mass. Thereafter, the solution is run for as much as $O(10)$ axial acoustic times to demonstrate that the steady-state solution is stable. Results given in Figure 2 show the steady normalized axial velocity, $u_S(x, r)/u_S(x, r = 0)$, and the radial velocity $v_S(x, r)$ profiles at different axial locations, $x = 0{\cdot}025, 0{\cdot}5$ and $1{\cdot}0$, when $M = 0{\cdot}05$ and $\mathrm{Re} = 3 \times 10^5$. Culick [12] profiles are virtually indistinguishable from the computed profiles, thus verifying the steady computational method. This result is anticipated because a low-Mach-number analysis predicts $O(M^2)$ differences between incompressible and compressible solutions.

A separate steady-state-flow solution is computed for each Mach number and Reynolds number in order to minimize the introduction of unwanted noise into the unsteady computations.

4.2. Unsteady flow computations

Once a converged steady-flow configuration is obtained for given M and Re, the flow is disturbed by imposing a sinusoidally fluctuating pressure on the exit plane, a model boundary

condition used previously by Vuillot and Avalon [1] and Tseng *et al.* [5]. The boundary condition at the exit plane is then

$$x = 1; \quad p = 1 + A \sin \omega t, \tag{25}$$

where ω is the dimensionless angular frequency and A is the amplitude of the pressure oscillation. The other boundary conditions are the same as those for steady flow computations.

The weakly nonlinear, asymptotic theory of Staab *et al.* [8] and Zhao *et al.* [17] employs the condition $A = O(M)$ which implies that the transient axial velocity field is of the same order of magnitude as the initial steady component. In the present computations the condition $A = M$ is sufficient to ensure that nonlinear processes will affect the evolution of the unsteady flow field.

The numerical code has been run approximately ten cycles ($t \approx 60$) after the pressure transient at the exit plane is turned on. It has been observed that no spurious numerical oscillations have developed.

The impact of grid size on solution accuracy has been evaluated systematically by repeating computations for a given set of physical parameters with increasingly large axial and radial grid point distribution. It is noted that the radial grid size is compatible with the integral transformation in (10) to assure resolution of the small-scale radial gradients that characterize the intense vorticity transient associated with u_{0V}. Results presented in Section 5 are independent of the grid structure to the accuracy cited.

The vorticity distribution in the flow field can be calculated by employing a numerical analogue to the velocity splitting described in the asymptotic analysis by (7) and (11) and used previously by Kirkkopru *et al.* [7]. The complete unsteady axial flow velocity is split into three parts;

$$u(x, r, t) = u_{SC}(x, r) + u_P(x, t) + u_V(x, r, t). \tag{26}$$

Here u_{SC} denotes the steady computational flow field which is known as an initial condition for the unsteady computations. The second component u_P is the analogue to the planar acoustic part of the flow field in (11). It is found as the difference between the unsteady axial speed u and the steady axial speed u_{SC} on the centerline of the tube $r = 0$, where the condition $u_V = 0$ is employed. The latter boundary condition is the numerical analogue to the asymptotic model requirement that $u_{0V} = 0$ on $r = 0$. This condition is derived from the properties of (16) on the axis, and the initial condition, $u_{0V} = 0$. The remaining part, u_V, is the analogue to u_{0V} in (11). It represents the transient, rotational, nonplanar (vortical) component of the unsteady axial flow speed, and can be used to describe the time history of the spatial distribution of unsteady vorticity in the cylinder.

Each of the components on the right side of (26) are compressible, viscous analogues to the terms in (7) and (11) of the previous section. For example, in the asymptotic analysis the steady and rotational components are described by incompressible equations and the former is inviscid as well. Similarly, the planar acoustic solution is compressible, but inviscid.

5. Discussion of results

The characteristics of the computational and asymptotic solutions and their comparison are considered in this section. Each of the results is given a physical interpretation to learn more about the acoustic field in the cylinder, its role in generating relatively intense transient vorticity at the injection surface and about the convection and diffusion of vorticity within the

internal flow. When appropriate, the computational results are considered in the context of insights gained from the asymptotic formulation in Section 3. More broadly, the model results provide a unique opportunity to study the dynamics of co-existing irrotational acoustics and rotational vorticity of similar magnitude in a well-defined internal flow configuration.

5.1. COMPUTATIONAL RESULTS

It is noted that for all cases to be discussed below the pressure solution has been found to be purely planar (x-dependent only), with no detectable transverse (radial) variation within computational accuracy. For example, numerical pressure values at $x = 0.5$ for three radial locations, $r = 0{\cdot}0, 0{\cdot}5$ and $1{\cdot}0$ are $p = 0{\cdot}9215026, 0{\cdot}9215026$ and $0{\cdot}921502$, respectively when $t = 30{\cdot}00$ for $M = 0{\cdot}1$, Re $= 3 \times 10^4$, $\omega = 1$ and $A = 0{\cdot}1$. This result for $\delta = 20$ supports the asymptotic prediction for the basic planar acoustic pressure distribution $P_0(x, t)$ in (15).

Axial pressure gradient and pressure time-response results are given in Figures 4 and 6 at an axial location $x = 0{\cdot}5$. It is noted that the former includes the steady, negative axial pressure gradient associated with the steady initial flow field u_{SC}, which has the value $-0{\cdot}07$. The amplitude of the transient is $O(M)$, which is in agreement with the expansion in (9). It is observed that the pressure change is delayed until about $t = 0{\cdot}5$, when the first acoustic signal originating from the exit plane, reaches the specified axial location. The startup process during the first few cycles is not purely harmonic and may contain the eigenfunction effects included in (15). However, the nonharmonic responses disappear quickly in the numerical result, leaving behind only the forced frequency response. This result has been seen before in all the generically related computational solutions [1, 2, 5–7] which have been carried out for velocity forcing at $x = 0$, for mass flow forcing at the exit plane as well as for the pressure forcing condition used in the current model.

Previous investigators have accepted the numerical results as accurate, in part because they focus on the pressure response in real solid rocket motor, which appears to be harmonic. None have provided the analytical acoustic solution for their specified boundary conditions in order to make the kind of comparison that is discussed in the present work. In fact, one can obtain the acoustic solution for each of the aforementioned IBVP's solved by computational methods to show that travelling-wave solutions are present. Their absence in the numerical solutions is almost certainly due to inadequate finite-difference representation of wave reflections at boundaries as discussed by Poinsot and Lele [28]. This point is reinforced by the recognition that viscous damping of planar acoustic waves will occur on a time-scale $t \gg O(10^2)$ for the Reynolds numbers considered here [21]. In this sense physically meaningful damping cannot annihilate the eigenfunction response during the intervals considered here. That does not preclude the possibility that numerical dissipation is a mathematical source of damping.

Recently, Hegab and Kassoy [27] employed characteristic boundary conditions [29] that preserve wave reflections on appropriate boundaries. The result for acoustic fields driven by transient sidewall injection, in contrast to the exit plane disturbance used here, retains eigenfunction responses on the acoustic time scale of the problem.

Although the eigenfunction responses cannot be reproduced by the current computational method, it is possible to use the solution to gain useful insights into the nonlinear dynamics of co-existing irrotational (acoustic) and rotational (vorticity) flow fields. Comparisons of the asymptotic results, including traveling-wave responses, with those from numerics can be used to quantify the relative impact of the eigenfunctions on the characteristics of the flow.

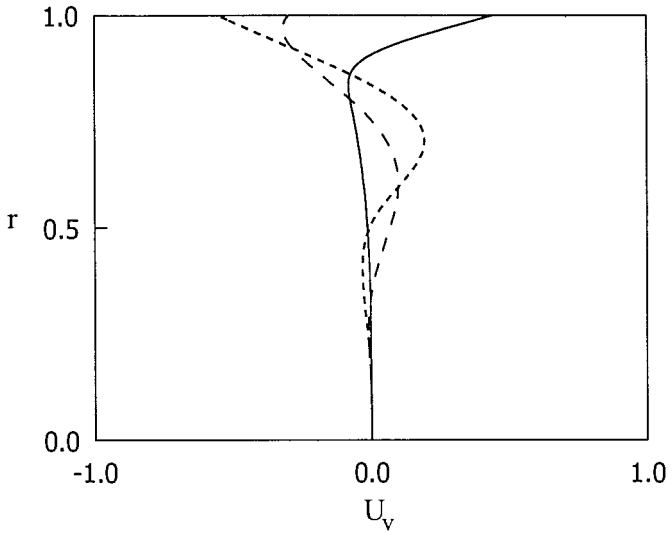

Figure 3. The radial variation of the unsteady axial flow speed, u_V, at $x = 0{\cdot}5$ when $t = 1{\cdot}50$ (solid line), $t = 10{\cdot}00$ (dotted line) and $t = 30{\cdot}00$ (dashed line) for $M = 0{\cdot}1$, $\delta = 20$, $\mathrm{Re} = 3 \times 10^4$, $\omega = 1$ and $A = M$.

The first results are for a relatively large Mach number, $M = 0{\cdot}1$. Figure 3 shows the radial variation of the instantaneous unsteady axial rotational flow speed u_V at $x = 0{\cdot}5$ for three values of time subsequent to initiating the disturbance in (25) at the exit plane; $t = 1{\cdot}50$, $10{\cdot}00$ and $30{\cdot}00$. The flow parameters, $M = 0{\cdot}1$ and $\mathrm{Re} = 3 \times 10^4$, are associated with an injection Mach number $M_i = M/\delta = 5 \times 10^{-3}$. The disturbance frequency is $\omega = 1{\cdot}0$, a non-resonant value smaller than the first natural frequency of the tube, $\omega_1 = \pi/2$, and $A = 0{\cdot}1$. One hundred and one grid points are used in the radial direction while 41 are used for axial resolution. One observes a strong radial velocity gradient extending out about $0{\cdot}15$ units from the wall at $t = 1{\cdot}50$ (solid line). This is the approximate radial distance travelled by the injected fluid during the short time interval $t = 1{\cdot}50$, as predicted by the asymptotic result in (19). The velocity gradient beyond that location is $O(M)$ smaller. As time evolves, the strong gradient penetrates further into the flow, filling most of the cylinder by $t = 30{\cdot}00$ (based on the numerical data itself). Equation (19) predicts that $r_F = 0{\cdot}99$ at $t = 30{\cdot}00$ in full agreement with the numerical results.

The spatial distribution of the rotational part of the unsteady axial flow velocity at each time in Figure 3 may be explained in physical terms by considering the interaction between the steady injected flow field and the planar acoustic disturbances created by the imposed pressure transient at the exit plane. The results in Section 3 suggest that particles injected from the sidewall ($r = 1$) at a specified axial location are affected by the time-response of the axial pressure gradient shown in Figure 4. Then, they are convected radially and axially, while acted upon by viscous diffusion on the r_2-length scale, which is small with respect to radius of the cylinder. Thus, the u_V profiles in Figure 3 reflect the time history of u_V generated on the wall $r = 1$, as described by (20), the subsequent invariant radial convection described by (16) and the convection-diffusion process given by (22).

Figure 5 shows the time history of u_P and u_V at the sidewall ($r = 1$) when $x = 0{\cdot}5$ for the parameters used in Figure 3. The no-slip boundary condition applied to (26) requires $u_V = -u_P$ on the sidewall boundary. It is seen from this figure that $u_V = u_P = 0$ for $t \lesssim 0{\cdot}5$ because the acoustic signal generated at $x = 1$ has not yet reached the location $x = 0{\cdot}5$. Once

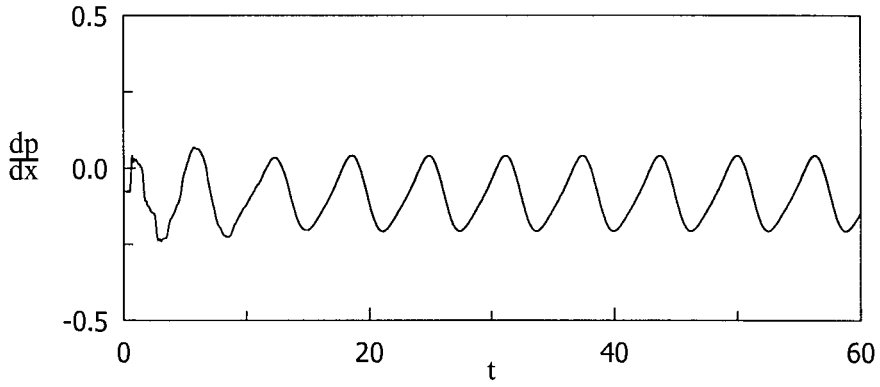

Figure 4. The time history of axial pressure gradient, $\partial p/\partial x$, at $x = 0{\cdot}5$, $r = 0{\cdot}9$ for $M = 0{\cdot}1$, $\delta = 20$, $\mathrm{Re} = 3 \times 10^4$, $\omega = 1$ and $A = M$.

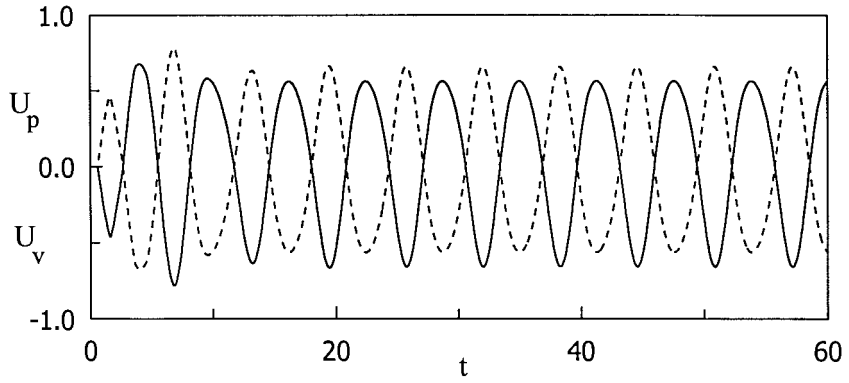

Figure 5. The time history of the planar part of the unsteady axial flow speed, u_P (solid line) and the unsteady vortical axial speed, u_V (dashed line) on the wall at $x = 0{\cdot}5$ for $M = 0{\cdot}1$, $\delta = 20$, $\mathrm{Re} = 3 \times 10^4$, $\omega = 1$ and $A = M$.

the signal arrives, u_V is generated at the wall by the interaction of the acoustic disturbance and the injected gas as predicted by (20). This is discussed in detail by Staab *et al.* [8] and Zhao *et al.* [17]. The presence of $u_V = O(1)$ on the sidewall demonstrates conclusively that a rotational axial velocity field is generated at the wall. Subsequently, the unsteady vorticity is convected towards the centerline as seen in Figure 3.

Figure 7 shows the spatial distribution of u_V at $x = 0{\cdot}5$ when $t = 1{\cdot}50$, $10{\cdot}00$ and $30{\cdot}00$ for $M = 0{\cdot}05$ (corresponding to the weaker injection, $M_i = 2{\cdot}5 \times 10^{-3}$) and $\mathrm{Re} = 3 \times 10^5$. The forcing frequency is $\omega = 1{\cdot}0$ and $A = 0{\cdot}05$. The large velocity gradient (vorticity) has penetrated about $0{\cdot}075$ units into the flow at $t = 1{\cdot}50$. At $t = 10{\cdot}00$ the penetration distance is about 50% of the tube radius, which agrees with the front location of $r_F = 0{\cdot}511$ from (19). At $t = 30{\cdot}00$ almost the entire cylinder is affected by transient vorticity. Compared to the results in Figure 3 for $M = 0{\cdot}1$, the spatial oscillation wavelengths in Figure 7 are considerably smaller, as implied by the asymptotic analysis. This occurs because injected fluid particles move a smaller radial distance in a given time interval when the wall injection speed is reduced from $M_i = 5 \times 10^{-3}$ to $2{\cdot}5 \times 10^{-3}$. One may also observe a small decrease in the wavelength of the oscillatory structure as the centerline is approached, which is a result of the vanishing radial flow speed as the centerline is approached.

Solution resolution requires 101 grid points in the radial direction 41 grid points in the axial direction. Near the injecting wall one wavelength of the u_V-spatial oscillation in Figure 7 contains approximately 35 radial grid points. Near the centerline, where the wavelength is smaller, approximately 10–15 grid points resolve the velocity gradients.

The third case studied is for $M = 0{\cdot}02$ ($M_i = 10^{-3}$), Re $= 3\times10^5$, $\omega = 1{\cdot}0$ and $A = 0{\cdot}02$. The results for the previous cases, $M = 0{\cdot}1$ and $M = 0{\cdot}05$, imply that the number of radial grid points should be doubled for this weak injection case, so that 201 equally spaced grid points are used to resolve the radial variation of u_V. The smoother axial variations are resolved by 41 axial grid points. Figure 8 shows the spatial variation of u_V at $x = 0{\cdot}5$ when $t = 3{\cdot}00$, 15·00 and 30·00. In each case the region of relatively large velocity gradients is reasonably well defined, so that one can identify how far the transient vorticity has penetrated into the flow.

Earlier computational results are based on grid clustering near the wall [1, 2, 5, 6] with a sparse distribution in the core. This was done to resolve an expected acoustic boundary layer adjacent to the injection surface. It is now understood from the asymptotic analyses [8, 17] that the injection speeds are sufficient to blow the viscous layer off the surface, so that viscous effects are distributed and persistent throughout the flow in the cylinder. The present work provides proper spatial resolution of the radial velocity distribution throughout the cylinder radius by including dense grid structure all across the cylinder.

It is noted that the magnitude of the gradient increases with decreasing M (compare Figures 3, 7 and 8), so that the absolute magnitude of the unsteady vorticity generated at the wall is much larger for small-Mach-number flows. Larger-time computations for the present IBVP have not been carried out. However, one can conclude from the works of Zhao and Kassoy [16], Zhao *et al.* [17] and Staab *et al.* [8] that the vorticity field will spread out towards the axis as time increases.

Figure 9 presents the axial and radial variation of unsteady vorticity,

$$\Omega = -\left[\frac{\partial u_V}{\partial r} - \frac{1}{\delta^2}\frac{\partial\,(v - v_S)}{\partial x}\right] \tag{27}$$

for $M = 0{\cdot}02$ at $t = 30$. The nondimensional vorticity is defined as $\Omega = \Omega'/\left(U'_R/R'\right)$, where Ω' is the dimensional vorticity. The primary contribution to Ω arises from the radial gradient of u_V in (27) when $\delta = 20$. This result agrees with the asymptotic prediction of Zhao *et al.* [17]. On this scale for vorticity the front, separating relatively large transient vorticity arising at the sidewall from the weaker variety in the core, is more sharply defined. The reduction in amplitude of Ω with distance from the sidewall occurs at all axial locations. It is also clear from Figures 3, 7 and 8 that the magnitude of the unsteady vorticity increases with decreasing Mach number.

The radial location of the front, r_F, separating the fluid region containing large transient vorticity from the one with much smaller vorticity associated with the steady flow conditions, can be obtained from Figures 3, 7 and 8 and more accurately from the actual numerical data used to generate each curve.

Table 1 shows the radial locations estimated from (19) and the asymptotic result, $r_F = 1 - Mt$, for small values of time compared to the computational values from the three Mach numbers discussed previously. One finds excellent agreement between the value of r_F from (19) and from the numerical results. Although $r_F = 1 - Mt$ gives good estimates near the wall, it yields unreasonable values for $r \gtrsim 0{\cdot}5$. This comparison helps to affirm the accuracy of the numerical solutions and in particular the calculation of u_V.

Table 1. The radial locations of the unsteady vortical axial velocity front, r_F, at different time levels for $M = 0{\cdot}02$, $0{\cdot}05$ and $0{\cdot}1$. The second and third columns present the estimates from $r_F = 1 - Mt$, valid for small times, and (19), respectively. Results in the last column have been found from Figures 3, 7 and 8.

Time	Front locations (r_F)		
t	$r_F = 1 - M_t$	Equation (19)	Numerical
	$M = 0{\cdot}02$		
3	0·94	0·94	0·93
15	0·70	0·69	0·67
30	0·40	0·44	0·44
	$M = 0{\cdot}05$		
1·5	0·93	0·92	0·92
10	0·50	0·51	0·50
30	−0·50	0·11	0·10
	$M = 0{\cdot}1$		
1·5	0·85	0·84	0·85
10	0·00	0·23	0·24
30	−2·00	0·01	0

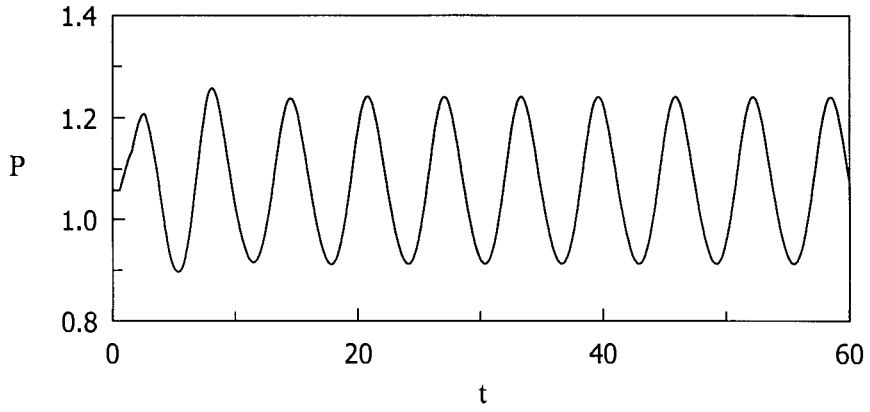

Figure 6. The time history of pressure at $x = 0{\cdot}5$ for the same parameters in Figure 5.

5.2. Comparisons with the asymptotic model

Figures 6 and 13a show numerical and asymptotic time histories of pressure, respectively, at the midcylinder for the parameter values $M = 0{\cdot}1$, $\delta = 20$, $\mathrm{Re} = 3 \times 10^4$, $A = M$ when $\omega = 1$. Amplitudes of the numerical and asymptotic unsteady pressure field are of the same order, $O(M)$, but differ quantitatively because of the absence of eigenfunctions in the former.

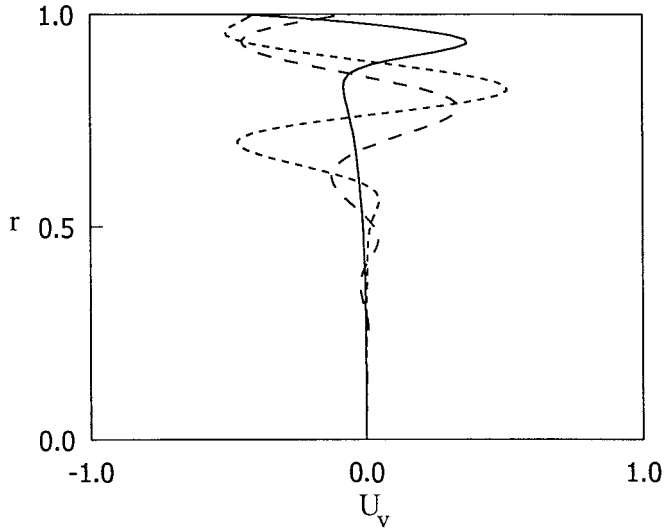

Figure 7. The radial variation of u_V at $x = 0{\cdot}5$ when $t = 1{\cdot}50$ (solid line), $t = 10{\cdot}00$ (dotted line) and $t = 30{\cdot}00$ (dashed line) for $M = 0{\cdot}05$, $\delta = 20$, $\mathrm{Re} = 3 \times 10^5$, $\omega = 1$ and $A = M$.

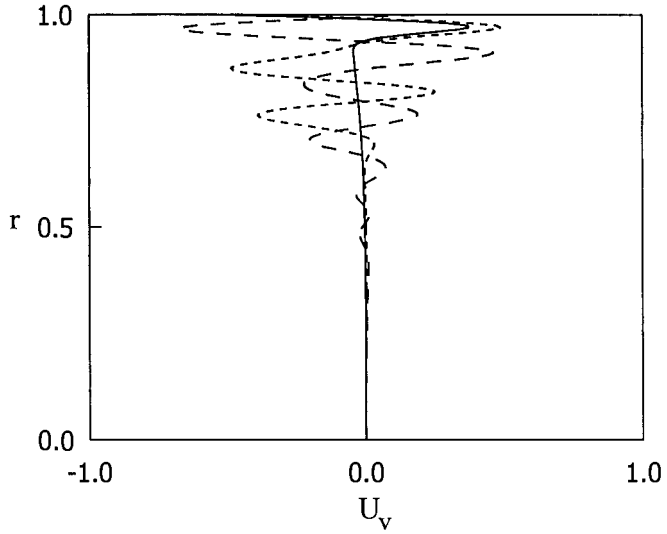

Figure 8. The radial variation of u_V at $x = 0{\cdot}5$ when $t = 3{\cdot}00$ (solid line), $t = 15{\cdot}00$ (dotted line) and $t = 30{\cdot}00$ (dashed line) for $M = 0{\cdot}02$, $\delta = 20$, $\mathrm{Re} = 3 \times 10^5$, $\omega = 1$ and $A = M$.

Figure 13b shows a comparison of numerical results from Figure 6 and the asymptotic pressure transient as calculated from (15) by omitting the eigenfunction contribution, that is, retaining only the forcing part in the form of $\sin \omega t$. This figure shows clearly that the magnitude and the frequency of both pressure variations are the same, except for a slight shift in time domain. The shift arises because the quasi-steady part of (15) cannot satisfy the initial condition. One can conclude from this comparison that the numerical code yields the correct forced pressure transient.

Figure 14a shows time variations of the axial acoustic velocities found from the asymptotic result in (15) (u_{0P}, dotted line) and from the full numerical solutions (u_P, solid line) using (26), an approximate analogue to (7) and (11). The qualitative differences in frequency

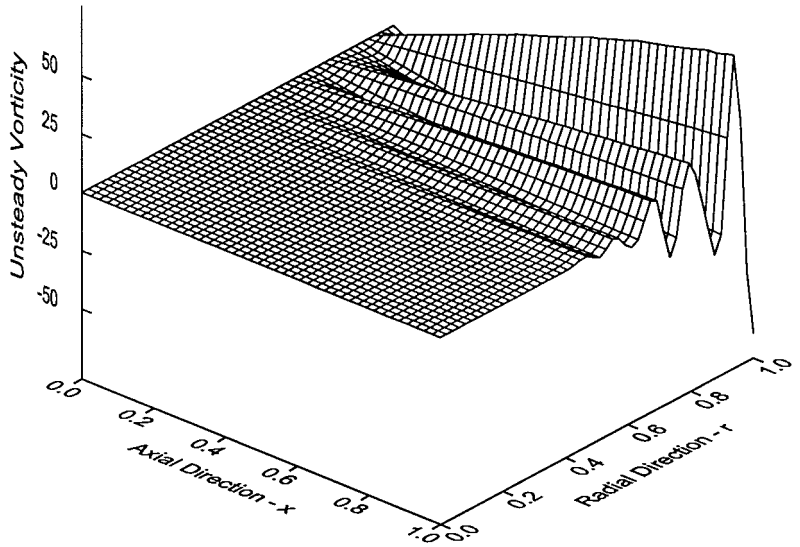

Figure 9. Spatial unsteady vorticity variation, Ω, defined in (27), throughout the cylinder at $t = 30{\cdot}00$ for $M = 0{\cdot}02$.

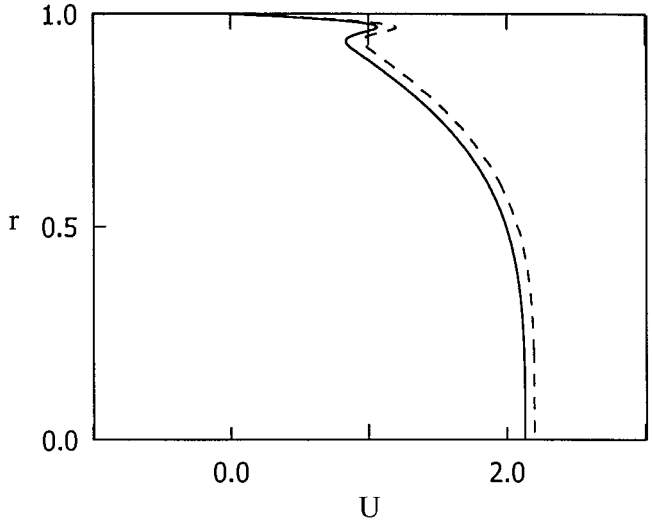

Figure 10. Comparison of the full numerical total axial velocity, u, (solid line) and the asymptotically found u (dotted line) at $x = 0{\cdot}5$ for $M = 0{\cdot}02$, $\delta = 20$, $\mathrm{Re} = 3 \times 10^5$, $\omega = 1$ and $A = 1$ at $t = 3$.

response and magnitude arise because the analytically derived acoustic field includes the effect of eigenfunctions.

Figure 14b shows a comparison between the numerical acoustic velocity (u_P) and the asymptotic acoustic velocity (u_{0P}) calculated from (15) by considering only the forced component in the form of cos ωt. Agreement of the amplitudes and the frequencies demonstrates that the acoustic velocity field response found by numerical computations provides a good representation of the forced mode. The time shift is similar to that seen in Figure 13b.

Comparisons of full computational and asymptotic results for rotational axial velocity are made for the case $M = 0{\cdot}02$ discussed in the previous section. This case features significant spatial structure in the radial direction at a given time.

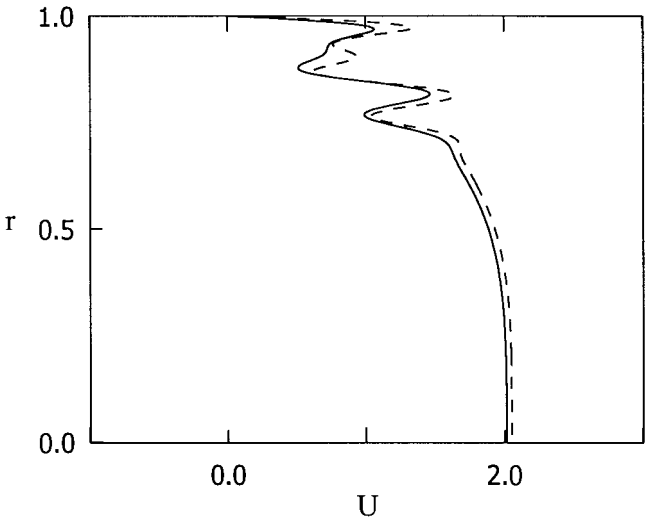

Figure 11. Similar comparison plot as in Figure 10 at $t = 15$.

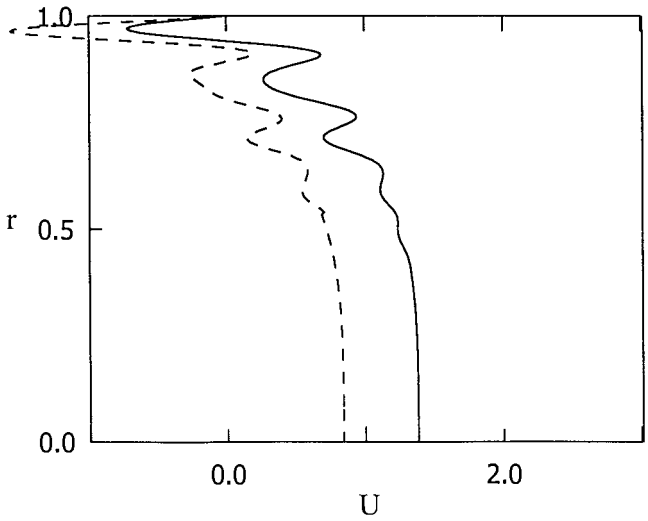

Figure 12. Similar comparison plot as in Figure 10 at $t = 30$.

Figures 10–12 show a series of comparisons of numerical and asymptotic axial velocity profiles at the axial midpoint of the cylinder, $x = 0{\cdot}5$, for the times $t = 3$, $t = 15$ and $t = 30$ when $M = 0{\cdot}02$, $\mathrm{Re} = 3 \times 10^5$, $A = M$ and $\delta = 20$ at the forcing frequency $\omega = 1$. The solid line represents the total instant axial velocity obtained from the computational solution of the IBVP and the dotted line indicates the asymptotic total axial velocity defined in (7). The comparisons in Figures 10–12 show that the numerical and asymptotic results yield qualitatively similar velocity profiles having the same number of spatial waves and the same shape in the radial direction. However, there exist quantitative differences between the values of numerical and asymptotic total axial velocities. These differences can be explained by recalling that the numerical acoustic velocity solution is missing a sizeable component associated with eigenfunction contribution to the acoustic field.

In order to understand the differences more fully it is useful to examine the behavior of the other velocity terms defined in (26). For example, Figure 2 shows that the numerical and asymptotic steady solutions are nearly identical. Finally the rotational fields should be compared.

It should be recalled that (20) shows that the unsteady vorticity created on the sidewall is sensitive to the unsteady axial pressure gradient. Figures 4 and 13c show the numerical and analytical acoustic axial pressure gradients, respectively, with differences due to the missing eigenfunctions in the numerical solution. This suggests that one can expect somewhat different rotational velocity solutions in each case.

Figures 15a–c show comparison of numerical and asymptotic unsteady rotational axial velocity profiles at the midpoint of the cylindrical chamber for the times $t = 3$, $t = 15$ and $t = 30$ for the same parameter values in Figures 10–12. The dotted line indicates the rotational axial velocity (u_{0V}) found from the solution of (22), and the solid line shows the numerically found analogous unsteady rotational axial velocity (u_V) depicted previously in Figure 8. The comparisons show that the solutions have the same qualitative behavior, including the same number of unsteady rotational velocity waves and similar decay rates in the radial direction. The differences in quantitative results include deviations on the sidewall ($r = 1$) and differences in peak values throughout the radial variation. Eigenfunctions are observed to have a larger effect near the sidewall than away from the boundary, where comparisons are quite good from a quantitative perspective. This improvement in quantitative comparison is likely due to the effects of diffusion, as defined in (22), that smooth out the radial gradient on the short radial scale as the fluid is convected into the cylinder and downstream. These results suggest that, even with a missing eigenfunction response, one can obtain a reasonably accurate prediction of the characteristics of the rotational field. Of course, improvements can be expected with a more accurate computational result.

6. Conclusions

The present computational and related asymptotic results show that:

(1) The small-time solutions to our initial-boundary-value problem are characterized by a well-defined front that separates the fluid region adjacent to the sidewall containing intense transient vorticity from the relatively weaker rotational flow (nearly the Culick solution in Figure 2) in the interior of the cylinder,

(2) Longer-time solutions show that the intense vorticity created at the injection surface is transported out into the cylinder core by the radial component of velocity. For sufficiently larger times transient vorticity fills the cylinder.

(3) The amplitude of the vorticity calculated from the initial-boundary-value problem is larger by a factor up to 100 than that considered in more traditional stability-based studies. In addition, for the larger disturbances considered in this work nonlinear axial convection is observed to affect the downstream distribution of vorticity [16, 17]. Results obtained from asymptotic analysis shows that the axial shear stress on the sidewall is $O(1/M)$, which can be quite significant.

(4) A reduction in the Mach number leads to more spatial oscillations in the radial variation of the flow velocity, implying smaller-length-scale phenomena. Spatial resolution of these rapid variations require a considerable number of radial grid points, particularly those away from the sidewall.

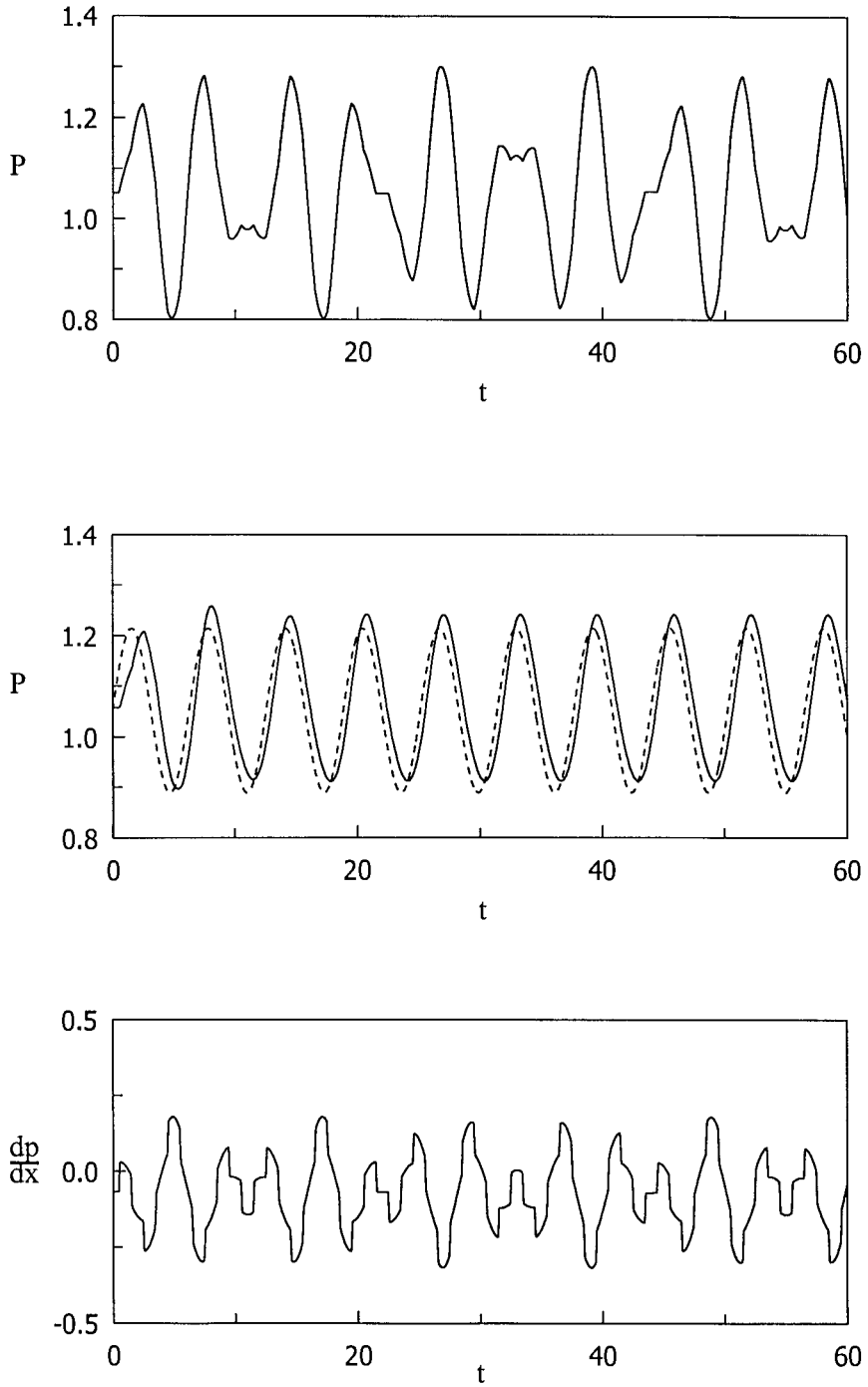

Figure 13. (a) Pressure time history found from (15), (b) Comparison of numerical P (solid line) and asymptotic P_0 (dotted line) found from (15) by considering only the forced mode, (c) axial pressure gradient time history obtained from Equation (15) at $x = 0{\cdot}5$ for the same parameters in Figure 6.

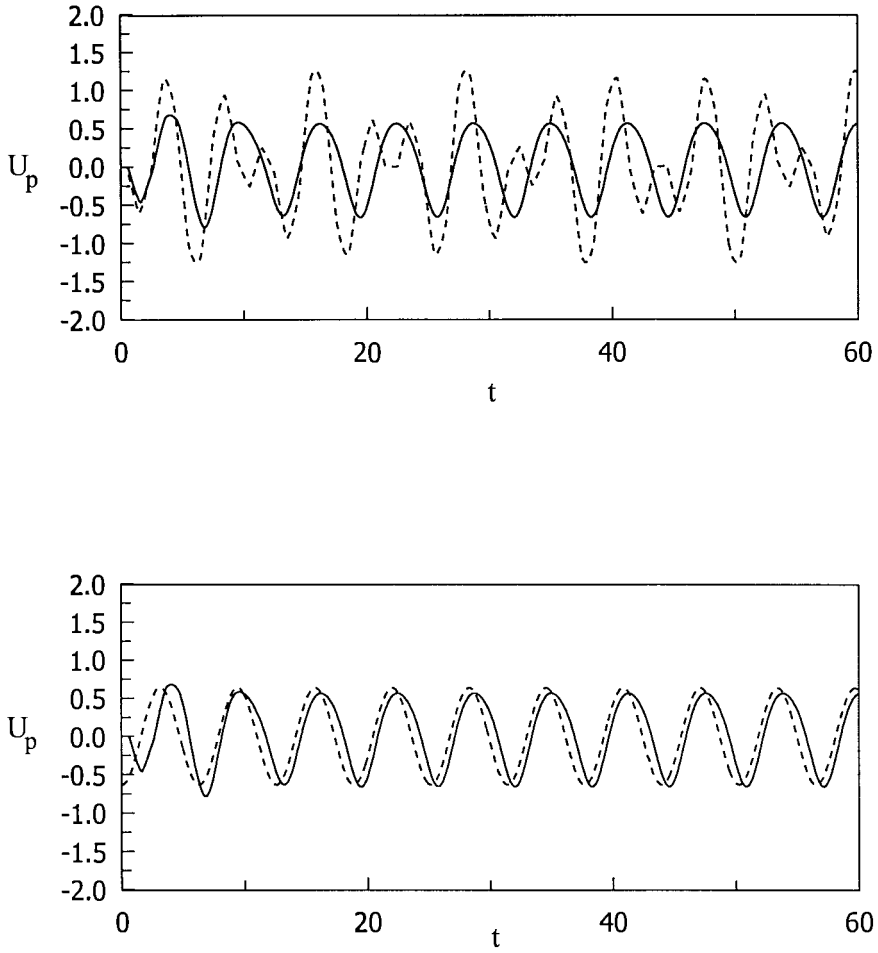

Figure 14. (a) The time history of the planar part u_{0P} of the total axial flow velocity found from Equation (15) (dotted line) and u_P extracted from full numerical calculations (solid line), (b) The time history of u_{0P} found from Equation (15) by considering only the forced mode (dotted line) and numerical u_p in Figure 14a (solid line) at $x = 0{\cdot}5$ for the same parameters in Figure 6.

(5) Acoustic eigenvalue responses that should be present in solutions to the defined mathematical models used previously [8, 16, 17] and the present work are not resolved by the numerical methods. However, in the present study eigenfunctions are present for sufficiently short times. (Figures 4 and 13c)

(6) The comparison of the numerically obtained pressure transient with the purely forced (quasi-steady) mode in the analytical acoustic solution (Equation 15) is excellent in terms of amplitude and frequency (Figure 13b).

(7) The computations in the present work are more accurate than those reported earlier [1, 2, 5, 6] because the analytically derived scaling is used to determine grid size and distribution. The present choices assure that the short wavelength processes in the radial spatial distributions, predicted by the analysis, are adequately resolved.

(8) The comparison between the nonlinear numerical results for rotational velocity and those obtained from the nonlinear asymptotic analysis is quite reasonable in the context of the differing acoustic pressure gradient transients obtained from each method.

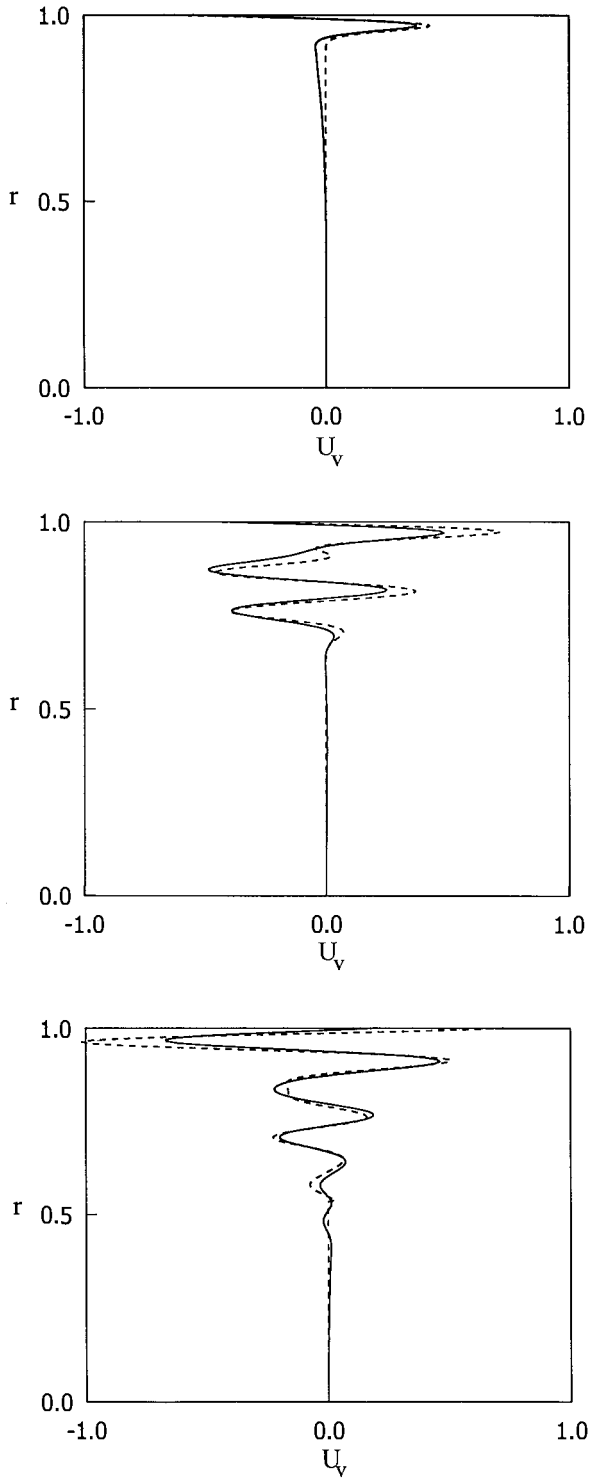

Figure 15. Comparison of the full numerical u_V (solid line) with the analytically found u_V from Equation (22) (dotted line) (a) at $t = 3{\cdot}00$, (b) at $t = 15{\cdot}00$ and (c) at $t = 30{\cdot}00$ for the same parameters in Figure 8.

Acknowledgements

This work has been supported by the Air Force Office of Scientific Research through a series grants and by a NATO–Collaborative Research Grant. The authors are grateful to the program managers for their continuing support of this project. The authors also appreciate the referees' suggestions for improving the content of the manuscript.

References

1. F. Vuillot and G. Avalon, Acoustic boundary layers in solid propellant rocket motors using Navier–Stokes equations. *J. Propuls. Power* 7 (1991) 231–239.
2. T.M. Smith, R.L. Roach and G.A. Flandro, Numerical study of the unsteady flow in a simulated solid rocket motor. AIAA 93-0112, Aerospace Science Meeting, Reno, Nevada, January 11–14 (1993)
3. R.S. Brown, A.M. Blackner, P.G. Willoughby and R. Dunlap, Coupling between acoustic velocity oscillations and solid propellant combustion. *J. Propuls. Power* 2 (1986) 428–437.
4. R.S. Brown, A.M. Blackner, P.G. Willoughby and R. Dunlap, Coupling between velocity oscillations and solid propellant combustion. AIAA 86-0531, AIAA Aerospace Sciences Meeting, January (1986).
5. C. Tseng, I.S. Tseng, W. Chu and V. Yang, Interactions between acoustic waves and premixed flames in porous chambers. AIAA 94–3328, Joint Propulsion Conference, Indianapolis, Indiana, June (1994).
6. T.S. Roh and V. Yang, Transient combustion responses of solid propellants to acoustic disturbances in rocket motors. AIAA-95-0602. 33rd Aerospace Sciences Meeting, Reno, NV (1995).
7. K. Kirkkopru, D.R. Kassoy and Q. Zhao, Unsteady vorticity generation and evolution in a model of a solid rocket motor. *J. Propuls. Power* 12 (1996) 646–654.
8. P.L. Staab,Q. Zhao, D.R. Kassoy and K. Kirkkopru, Coexisting acoustic-rotational flow in a cylinder with axisymmetric sidewall mass addition. *Phys. Fluids* B11 (1999) 2935–2951.
9. G.A. Flandro, Solid propellant admittance correction. *J. Sound Vibr.* 36 (1974) 297–312.
10. G.A. Flandro and R.L. Roach, Effects of vorticity production on acoustic waves in a combustion chamber. Final Technical Report, AFOSR-90-0159 (1992).
11. G.A. Flandro, Effects of vorticity on rocket combustion stability. *J. Propuls. Power* 11 (1995) 607–625.
12. F.E.C. Culick, Rotational axisymmetric mean flow and damping of acoustic waves in a solid propellant rocket. *AIAA J.* 4 (1966) 1462–1464.
13. J. Majdalani and W. Van Moorhem, Multiple-scales solution to the acoustic boundary layer in solid rocket motors. *J. Propuls. Power* 13 (1997) 186–193.
14. J. Majdalani, G.A. Flandro and T.S. Roh, Implications of unsteady analytical flowfields on rocket combustion stability. AIAA-98-3698, 34th AIAA/ASME/SAE/ASEE Joint Propulsion Conference, Cleveland, OH (1998).
15. J. Majdalani, Characterization of the laminar boundar layer in solid rocket motors. AIAA-98-3699, 34th AIAA/ASME/SAE/ASEE Joint Propulsion Conference, Cleveland, OH (1998).
16. Q. Zhao and D.R. Kassoy, The generation and evolution of unsteady vorticity in a solid rocket engine chamber. AIAA 94-0779, Aerospace Sciences Meeting, Reno, Nevada, January (1994).
17. Q. Zhao, P.L. Staab, D.R. Kassoy and K. Kirkkopru, Acoustically generated vorticity in an internal flow. *J. Fluid Mech.* 413 (2000) 247–285.
18. R.W. MacCormack, The effect of viscosity in hypervelocity impact cratering. AIAA 69-354, Cincinnati, OH (1969).
19. J.D. Cole and J. Aroesty, The blowhard problem-inviscid flows with surface injection. *Int. J. Heat Mass Transfer* 11 (1968) 1167–1183.
20. P.A. Lagerstrom, Laminar Flow Theory. In: F.K. Moore (ed.), *Theory of Laminar Flows*. Princeton (N.J.): Princeton University Press (1964) chap B, pp 20–285.
21. L.D. Landau and E.M. Lifshitz, *Fluid Mechanics*. New York Pergamon Press, (1959) 539 pp.
22. J. Kevorkian and J.D. Cole, *Perturbation Methods in Applied Mathematics*. New York: Springer-Verlag (1985) 558 pp.
23. F. Vuillot, Vortex-shedding phenomena in solid rocket motors. *J. Propuls. Power* 11 (1995) 626–639.
24. G. Casalis, G. Avalon and J. P. Pineau, Spatial instability of planar channel flow with fluid injection through porous walls. *Phys. Fluids* 10 (1998) 2558–2568.

25. G. Avalon, G. Casalis and J. Grifford, Flow instabilities and acoustic resonance of channels with wall injection, AIAA 98-3128, 34th AIAA/ASME/SAE/ASEE Joint Propulsion Conference, Cleveland, OH (1998).
26. G. I. Taylor, Fluid flow in regions bounded by porous surfaces. *Proc. R. Soc. London A*234 (1956) 456–475.
27. A.K. Hegab and D.R. Kassoy, Internal flow temperature dynamics in a channel with time-dependent mass injection, submitted to *J. Propuls. Power* (2001).
28. T.J. Poinsot and S.K. Lele, Boundary conditions for direct simulations of compressible viscous flows. *J. Comp. Phys.* 101 (1992) 104–129.
29. K.W. Thompson, Time dependent boundary conditions for hyperbolic systems II. *J. Comp. Phys.* 89 (1990) 439–461.